

This is the accepted manuscript made available via CHORUS. The article has been published as:

# Multifunctional acoustic metasurface based on an array of Helmholtz resonators

Yifan Zhu and Badreddine Assouar

Phys. Rev. B **99**, 174109 — Published 20 May 2019

DOI: [10.1103/PhysRevB.99.174109](https://doi.org/10.1103/PhysRevB.99.174109)

# Multifunctional acoustic metasurface based on Helmholtz resonators array

Yifan Zhu<sup>\*</sup> and Badreddine Assouar<sup>\*</sup>

*Institut Jean Lamour, CNRS, Université de Lorraine, Nancy, France.*

## Abstract

We demonstrate multifunctional acoustic metasurfaces (MAMs) that can simultaneously realize the same functionality or multiple different functionalities at multiple tunable frequencies. The fundamental physical mechanism is based on designing supercell of Helmholtz resonators (HRs) with multiple resonances operating at different frequencies. We theoretically, numerically and experimentally demonstrate the achievement of multiple functionalities by the proposed designed metastructure, which produces extraordinary reflection at different angles and different acoustic focusing localizations under the same normal incidence. Our finding paves the way towards multifunctional compact acoustic devices and can lead to pragmatic contemporary applications such as multiple beam shaping, or functional device with special dispersion property.

**Keywords:** Acoustic Metasurfaces, Acoustic Metamaterials, Multifunctionality, Helmholtz Resonators

**Corresponding authors:**

\*yifan.zhu@univ-lorraine.fr

\*badreddine.assouar@univ-lorraine.fr

## I. INTRODUCTION

Acoustic metasurfaces, in analogy to optical metasurfaces [1] which firstly have been proposed in 2011, are a kind of ultrathin metamaterials based on the generalized Snell law. These innovative designed metastructures provide a new way to manipulate wavefront freely by introducing abrupt changes of acoustical phases. This breaks the dependence on the propagation effect and enables molding wavefront into arbitrary shapes with subwavelength resolution. Recently, a flurry of researches has revealed acoustic metasurfaces as suitable materials to control sound propagation, leading to novel engineering applications in acoustics. Different extraordinary and unique functionalities have been realized by the acoustic metasurfaces [2], such as extraordinary refraction/reflection [3], planar focusing [4], non-diffracting beams [5], sound absorption [6], and so on, opening an exciting application field for wave manipulation in particular, and for physical acoustics, at large.

Classical design of metasurface usually focuses on the single structure unit to realize  $0-2\pi$  phase range [3]. However, some previous works have considered the advantages of the unique properties of the supercells. For example, by manipulating the multiple reflection directions in a supercell consisting of two gradient metasurfaces, asymmetric sound transmission is realized in a tunnel structure [7]. Li *et al.* have used the hybrid resonances of Helmholtz resonators (HRs) array to realize transmitted phase modulation [4, 8]. Amin *et al.* have explored the resonant mechanism of a binary-groove supercell structure to realize a transformational metascreen [9]. Ma *et al.* have demonstrated multi-frequency sound absorption by coupling three absorptive units in a supercell [6]. Liu *et al.* have demonstrated

the apparent negative reflections explained by different high-order diffractions of the supercell [10], while Li *et al.* and Liu *et al.* have demonstrated sound absorption [11] and energy harvesting [12] via coupled HRs, respectively.

In our previous work, we have designed a supercell with four HRs for four different targeted frequencies to broaden the bandwidth of a metasurface-diffuser [13]. Inspired by this work, we consider that if the designed phase profiles are changed from diffuse reflections to other functionalities, beam steering with multiple degrees of freedom can be achieved. In this paper, we present a demonstration of multifunctional (or multi-frequency) acoustic metasurfaces (MAMs) that can simultaneously realize the same or multiple different functionalities at multiple frequencies. The functionality of the proposed metasurface can be tailored at different working frequencies, that can be tunable instead of operating at only harmonic wave frequencies [14].

Comparing to membrane-type demultiplexing acoustic metasurface [15], the MAM designed based on HR arrays [4, 8, 11-13, 16-20] features simple structure and steady acoustic properties (amplitude and phase responses) which benefit for practical applications. Here, we also present the analytical derivation for the metastructure supercell, which agrees well with the simulated results. As a typical example, we demonstrate the achromatic extraordinary reflection/focusing and other mixed functionalities at different frequencies. Our finding can open a new degree of freedom for tunable wave manipulation by metasurfaces and has the capability to break the limitation of conventional structured acoustic metasurface that has only one degree of freedom. This could lead to unusual physical effects and

applications such as multiple beam shaping.

## II. SUPERCELL DESIGN AND THEORY

In the following, we show the two-dimensional (2D) supercell design that can respond to three different frequencies, *viz.*,  $f_1 - f_3$ . Figure 1 shows the schematic diagram of the supercell of the MAM consisting of three HRs with different heights. The combination of HRs presents a suitable approach to generate multiple acoustic resonances. As shown in Fig. 1(a), the geometrical parameters in the unit cell are set as: the period of the unit cell is  $d = 0.05\text{m}$ , the width of the three cavities are  $d_1 = 0.014\text{m}$ , their heights are fixed as  $h_1 = 0.036\text{m}$ ,  $h_2 = 0.018\text{m}$ , and  $h_3 = 0.009\text{m}$ , respectively. The thickness of the side wall between two HRs and the thickness of the neck are both  $0.002\text{m}$ . The neck widths of the three HRs, *viz.*,  $w_1$ ,  $w_2$ , and  $w_3$  are different to modulate the phase response of the unit cells at  $f_1 - f_3$ , respectively. The total acoustic impedance of  $n$ th ( $n=1,2,3$ ) HR ( $\text{HR}_n$ ) can be expressed as [21-23]:

$$Z_n = Z_{Sn} + Z_{Cn} \quad (1)$$

Where  $Z_{Sn}$  is the acoustic impedance induced by the neck and body of  $\text{HR}_n$ , which is expressed as:

$$Z_{Sn} = i(\omega_n M_n - \frac{1}{\omega_n C_n}) \quad (2)$$

Where  $\omega_n = 2\pi f_n$  is the angular frequency,  $M_n = \rho_0 l_e / w_n$  and  $C_n = h_n d_1 / \rho_0 c_0^2$  are acoustic mass and acoustic compliance [21-22] (or called as acoustic capacitance [23]) of air

in the  $HR_n$ , respectively, which is characterized as inductance and capacitance in effective circuit model [21-23].  $\rho_0 = 1.21 \text{ kg/m}^3$  and  $c_0 = 343 \text{ m/s}$  are the density of air and the sound speed in the air, respectively.  $l_e = l + \Delta l$  is the effective length of the neck with  $l = 0.002 \text{ m}$  being the length of the neck, and  $\Delta l$  being the correctional length induced by added acoustical mass due to radiation (see Supplemental Material [24]).

$Z_{Cn}$  is the acoustic impedance induced by the coupling of the neighbouring HRs. For example,  $Z_{C1}$  can be expressed as [22]:

$$Z_{C1} = \frac{Z_{12}^2}{Z_{S2}} + \frac{Z_{13}^2}{Z_{S3}} \quad (3)$$

Where  $Z_{12}$  ( $Z_{13}$ ) are the mutual impedances between  $HR_1$  and  $HR_2$  ( $HR_1$  and  $HR_3$ ). The values of mutual impedance [22] are large when the HRs are placed in close proximity and the resonant frequencies of neighboring two HRs are close together (see Supplemental Material [24]). Thus, the designed resonant frequencies of HRs cannot be very close to decrease the coupling effects.

Because the considered supercell consists of three different unit cells, and the transverse size of the supercell is still subwavelength, we use effective circuit model to characterize it, as illustrated in Fig. 1(b). The impedance of one HR is the sum of acoustic compliance, acoustic mass, and the term  $Z_{Cn}$  induced by the coupling effect of HRs. Then, the acoustic impedance of the supercell is obtained by shunt-wound three impedances of HRs, which is expressed as:

$$Z = \frac{1}{1/Z_1 + 1/Z_2 + 1/Z_3} \quad (4)$$

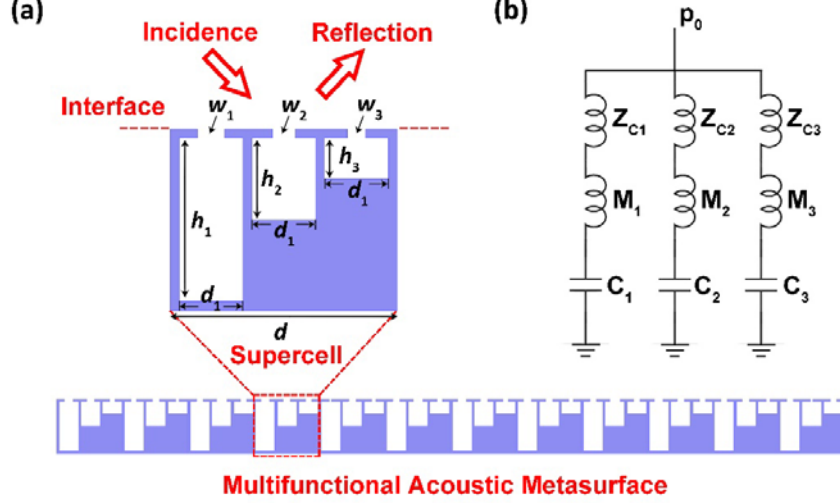


FIG. 1. (a) 2D schematic diagram of the supercell of multifunctional acoustic metasurface. A supercell is consisting of three cavities with different depths. (b) The effective circuit model of the proposed supercell of metasurface.

Based on the acoustic impedance of supercell, the phase shift of the supercell can be approximately expressed as [13]:

$$\phi = \text{angle}[(Z - \rho_0 c_0 / d) / (Z + \rho_0 c_0 / d)] \quad (5)$$

We can then modulate the phase within  $0 - 2\pi$  for three frequencies  $f_1 - f_3$  (1340Hz, 2040Hz, and 3000Hz) by solely tuning the geometrical parameters  $w_1$ ,  $w_2$ , and  $w_3$  as the simulated results shown in Figs. 2(a-c). For example, at 1340Hz, the reflection phase is only determined by  $w_1$ , but unrelated to  $w_2$  or  $w_3$ , because the frequency resonance at 1340Hz is only coupled with the deepest cavity. The three different cavities are designed to match to the three targeted frequencies. Analogously,  $w_2$  and  $w_3$  are tailored to control the phase at 2040Hz, and 3000Hz, respectively. The independent control of phase by one parameter will

be explained later. Figures 2(a-c) also display the analytical results calculated by Eq. (5), which agree well with the simulated ones, validating the proposed analytical model.

It's worth mentioning that, the key point in supercell design is to first select three distinct heights of the cavities  $h_1 - h_3$ . Then the targeted frequencies  $f_n$  are obtained as the resonant frequency of three cavities with fixed necks width  $w_n = 2\text{mm}$ . After that we can change  $w_n$  around 2mm to modulated the reflected phases for three frequencies, respectively, since the phase shifts are obvious around the resonances [13]. The resonant condition of  $\text{HR}_n$  is:  $Z_n = Z_{Sn} + Z_{Cn} = 0$ , which means the impedance at resonant circuit branch is zero. When the values of three  $h_n$  are not close together, the coupling effects of HRs ( $Z_{Cn}$  value is small) is suppressed (see Supplemental Material [24]), and the resonant frequency of  $\text{HR}_n$  is analytically expressed as:

$$f_n = \frac{1}{2\pi} \sqrt{\frac{1}{M_n C_n}} \quad (6)$$

We show the simulated and analytical (Eq. 6) relationship between  $h_n$  and  $f_n$  (the resonant frequencies with  $w_n = 2\text{mm}$ ) in Fig. 2(d). The  $f_1 - f_3$  (1340Hz, 2040Hz, and 3000Hz) corresponding to  $h_1 - h_3$  (0.036m, 0.018m, and 0.009m) are marked on the curve. The insets in Fig. 2(d) display the acoustic pressure amplitude distribution of the eigenmodes at  $f_1 - f_3$ , verifying that each frequency resonance is coupled with only one cavity with corresponding  $h_n$ , respectively.

We can then numerically explain the independent control at each frequency from Eq. (4). In general case, the phase response is related to all geometrical parameters of three cavities (*viz.*  $Z_1, Z_2$ , and  $Z_3$ ) due to the coupled resonance in the supercell. However, in our design,



the operating frequency  $f_n$  is near the resonant frequency of  $\text{HR}_n$  when changing its neck width  $w_n$ . In this case, the value of  $Z_n$  is relatively small. It makes Eq. (4) be approximate to  $Z \approx 1/(1/Z_n + 0 + 0) = Z_n$  (this means the incident wave is only coupled with one HR, but the HRs are decoupled with each other), leading to the independent phase modulation by only one parameter (*viz.*  $w_n$ ).

In the following, the acoustic loss in the metastructure is evaluated. Figure 2(e) shows the simulated reflected amplitude of the supercell with different  $w_n$  values at different frequencies. The loss is induced by thermal-viscous effect in the cavities when the neck widths  $w_n$  are narrow (comparable with the thickness of boundary layer  $d_{\text{visc}} = 0.22\text{mm} \times \sqrt{100/f_n}$ ). The maximum loss appears at the resonance of the HRs. Considering the thermal-viscous loss, the average reflected acoustic energy of MAM is larger than 0.85, verifying the practicability of the HRs array.

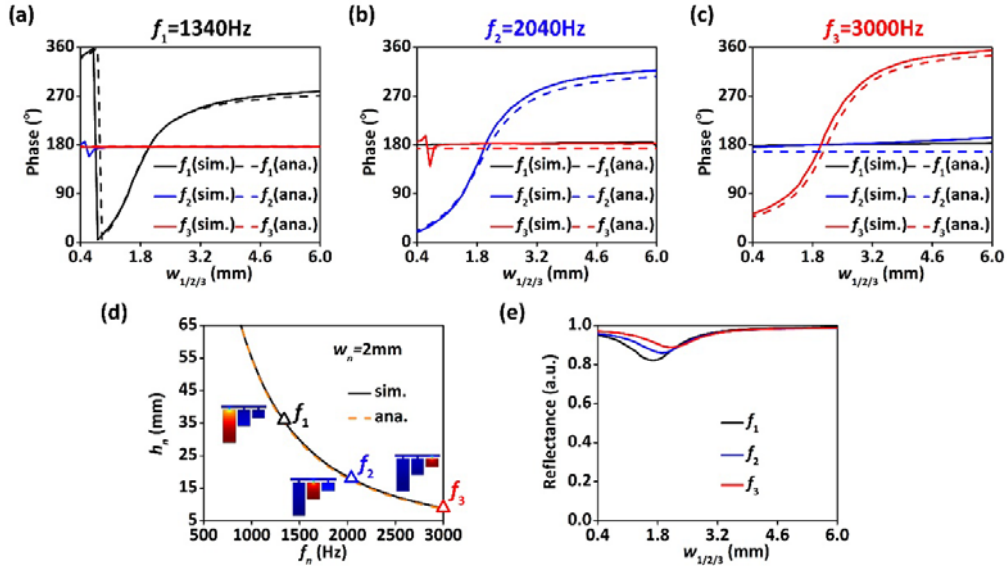


FIG. 2. (a-c) The simulated (sim.) and analytical (ana., calculated by Eq.(5)) phase responses

diagram for  $f_1 = 1340\text{Hz}$ ,  $f_2 = 2040\text{Hz}$ , and  $f_3 = 3000\text{Hz}$ , respectively. (d) The simulated (sim.) and analytical (ana., calculated by Eq. (6)) relationship between the height of the cavity and the targeted frequencies with  $w_n = 2\text{mm}$ . The targeted frequencies can be chosen within about 900Hz-3000Hz. The insets show the acoustic pressure amplitude distribution of the eigenmodes at three targeted frequencies, indicating that each resonance is coupled with only one cavity, respectively. (e) The reflectance of the supercell with different  $w_n$  values for different frequencies. The loss is induced by thermal-viscous effect in the cavities.

### III. ACHROMATIC ACOUSTIC METASURFACE

We use the designed supercell to build the multifunctional metasurface. As basic designs, Fig. 3 shows the two metasurface that have the same extraordinary reflections or the same focal positions at three frequencies, respectively, *viz.*, achromatic acoustic metasurface (AAM). It is the analogy of the optical one [25] but has not been realized yet in acoustics. AAM can be regarded as a special case of MAM that has the same functionality at different frequencies. In order to design an AAM, the phase profiles for  $f_n$  are expressed in Eqs. (7) and (8), respectively [3, 26].

$$\phi_n = k_n x (\sin \theta_i - \sin \theta_r), \quad (7)$$

$$\phi_n = k_n \left[ \sqrt{(x - x_0)^2 + y_0^2} - \sqrt{x_0^2 + y_0^2} \right], \quad (8)$$

where  $\theta_{i/r}$  is incidence/reflection angles,  $k_n = w_n / c_0$  is wave number of  $n$ th frequencies,  $(x_0, y_0)$  is the focal position. The calculated phase profiles by Eqs. (7) and (8) are shown in Figs. 3(a) and 3(c). We have set the  $-45^\circ$  extraordinary reflection that requires linear phase

response  $\phi_n = \sqrt{2}k_n x / 2$  as shown in Fig. 2(a). Because the wave numbers  $k_n$  are different for the three frequencies, the corresponding phase distributions are different but are all linear. Similarly, we have set the focal position as coordinate (0m, 0.6m) for achromatic acoustic focusing. Hyperboloidal phase distributions  $\phi_n = k_n(\sqrt{x^2 + 0.36} - 0.6)$  are required, as shown in Fig. 3(c).

The simulated acoustic fields for extraordinary reflection and acoustic focusing are shown in Figs. 3(b) and 3(d), respectively. Throughout this work, the numerical simulations are performed by the finite element method based on commercial software COMSOL Multiphysics 5.2a. The arrows indicate the incidence/reflection directions and the focusing positions. The field patterns at the three frequencies clearly evidence the achievement of the achromatic extraordinary reflection and achromatic acoustic focusing. It is noted that the focal spot is different due the diffraction effects at different frequencies.

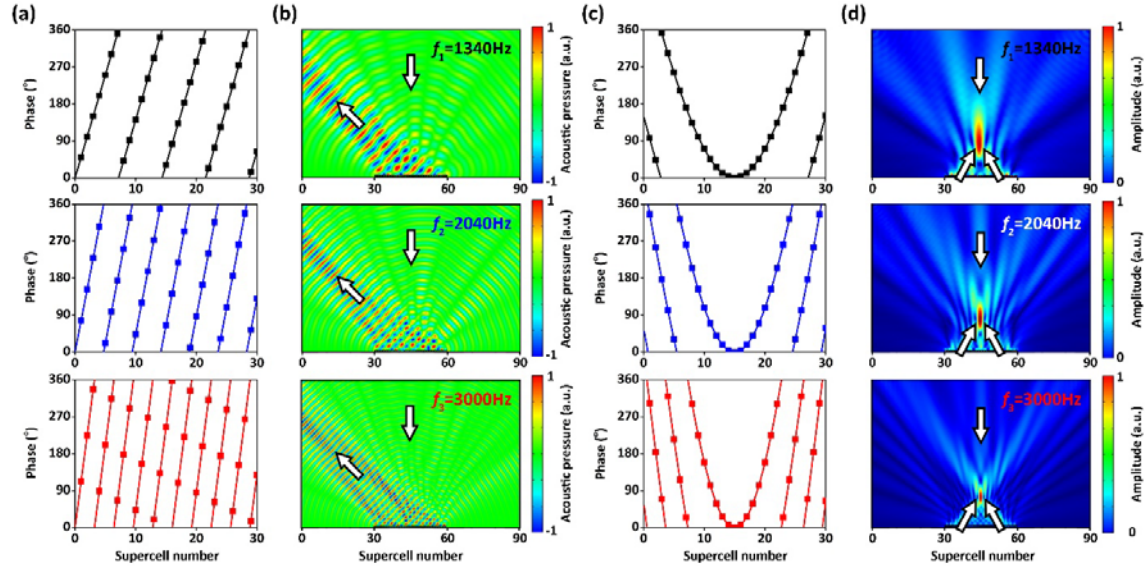


FIG. 3. (a) The phase responses for achromatic  $-45^\circ$  extraordinary reflection at three

frequencies. Linear phase distributions  $\phi_n = \sqrt{2}k_n x / 2$  are applied on the interface. (b) The simulated results for achromatic  $-45^\circ$  extraordinary reflection at three frequencies. (c-d) The corresponding results for achromatic acoustic focusing at (0m, 0.6m). Hyperboloidal phase responses  $\phi_n = k_n(\sqrt{x^2 + 0.36} - 0.6)$  are applied on the interface. The arrows indicate the incidence/reflection directions and the focusing positions.

#### IV. MULTIFUNCTIONAL ACOUSTIC METASURFACE

In this section, we show the real design of MAM with different functionalities at different frequencies. Figure 4 shows two MAM designs. In Figs. 4(a) and 4(b), with our designed metasurface under a normal incidence, we have realized  $-45^\circ$  extraordinary reflection, acoustic focusing at coordinate (0m, 1m) and  $45^\circ$  extraordinary reflection at 1340Hz, 2040Hz, 3000Hz, respectively. The calculated phase profiles from Eqs. (7) and (8) are  $\phi_1 = \sqrt{2}k_1 x / 2$ ,  $\phi_2 = k_2(\sqrt{x^2 + 1} - 1)$ ,  $\phi_3 = -\sqrt{2}k_3 x / 2$ , respectively, as show Fig. 4(a). Similarly, in Figs. 4(c) and 4(d), we have realized acoustic focusing at different focal points  $(-0.4\text{m}, 0.6\text{m})$ ,  $(0\text{m}, 0.6\text{m})$ , and  $(0.4\text{m}, 0.6\text{m})$  at 1340Hz, 2040Hz, 3000Hz, respectively. The phase profiles deduced from Eqs. (5) and (6) are  $\phi_1 = k_1(\sqrt{(x + 0.33)^2 + 0.36} - 0.686)$ ,  $\phi_2 = k_2(\sqrt{x^2 + 0.36} - 0.36)$ ,  $\phi_3 = k_3(\sqrt{(x - 0.33)^2 + 0.36} - 0.686)$ , respectively, as show Fig. 4(c). The numerical results in Figs. 4(b) and 4(d) suggest that the mixed functionalities can be freely tailored, showing the real added value of our design of the MAMs. The different functionalities can be designed solely due to the locally resonant property of each unit cell. Based on the same mechanism, more functionalities could be realized with one metasurface,

such as diffuse reflection, self-bending beam, or sound absorption.

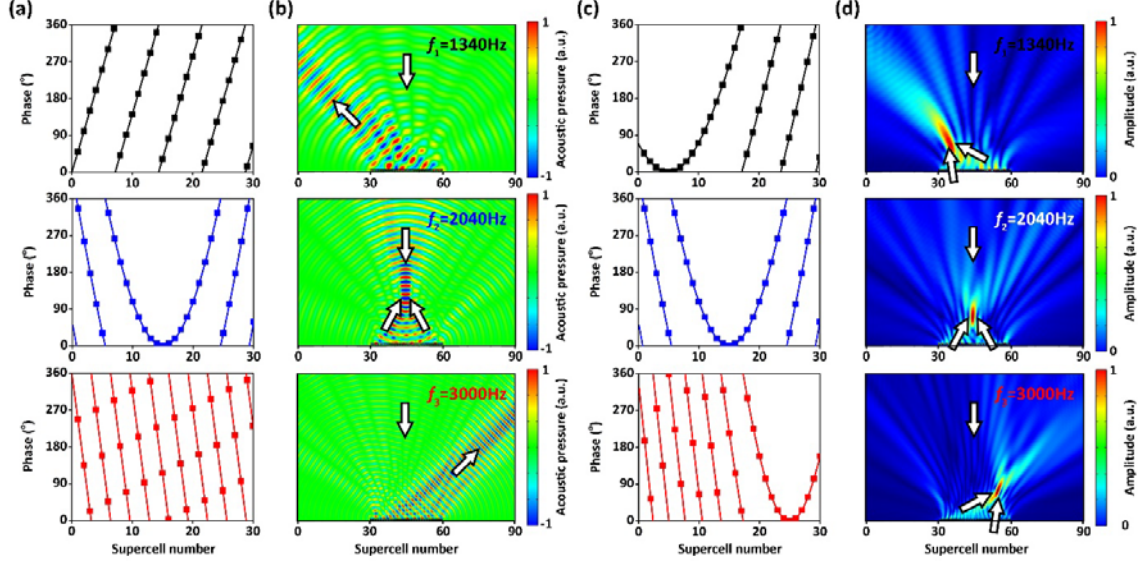


FIG. 4. (a) The different phase responses of MAM at three frequencies:  $\phi_1 = \sqrt{2}k_1x/2$ ,  $\phi_2 = k_2(\sqrt{x^2+1}-1)$ ,  $\phi_3 = -\sqrt{2}k_3x/2$ . (b) The simulated results of MAM at three frequencies, for  $-45^\circ$  extraordinary reflection, acoustic focusing at coordinate (0m, 1m) and  $45^\circ$  extraordinary reflection. (c) The different phase responses of another MAM at three frequencies:  $\phi_1 = k_1(\sqrt{(x+0.33)^2+0.36}-0.686)$ ,  $\phi_2 = k_2(\sqrt{x^2+0.36}-0.36)$ ,  $\phi_3 = k_3(\sqrt{(x-0.33)^2+0.36}-0.686)$ . (d) Acoustic focusing with different focal positions ((-0.33m, 0.6m), (0m, 0.6m), and (0.33m, 0.6m)) at three frequencies. The arrows indicate the incidence/reflection directions and the focusing positions.

## V. EXPERIMENTAL DEMONSTRATION

We have carried out experimental fabrication and analysis to evidence the functionalities of the investigated metasurface. Figure 5 shows the experimental

demonstration of the proposed MAM. We have fabricated the MAM sample (The photograph is shown in Fig. 5(a)) for acoustic focusing with different focal positions ((1.67m, 0.6m), (2m, 0.6m), and (2.33m, 0.6m)) at 1340Hz, 2040Hz, 3000Hz, respectively. Figure 5(b) shows the simulated and measured acoustic pressure distributions of the acoustic focusing at three frequencies. The measured results of the acoustic pressure fields at the given region marked in the figure are shown in the inset. In the experiment, the loudspeaker is put 3m away from the sample to mimic a plane wave. Figure 3(c) illustrates the simulated and measured acoustic pressure amplitude distributions at the line of  $y=0.6m$ . The experimental results agree well with the simulated ones with a reasonable error.

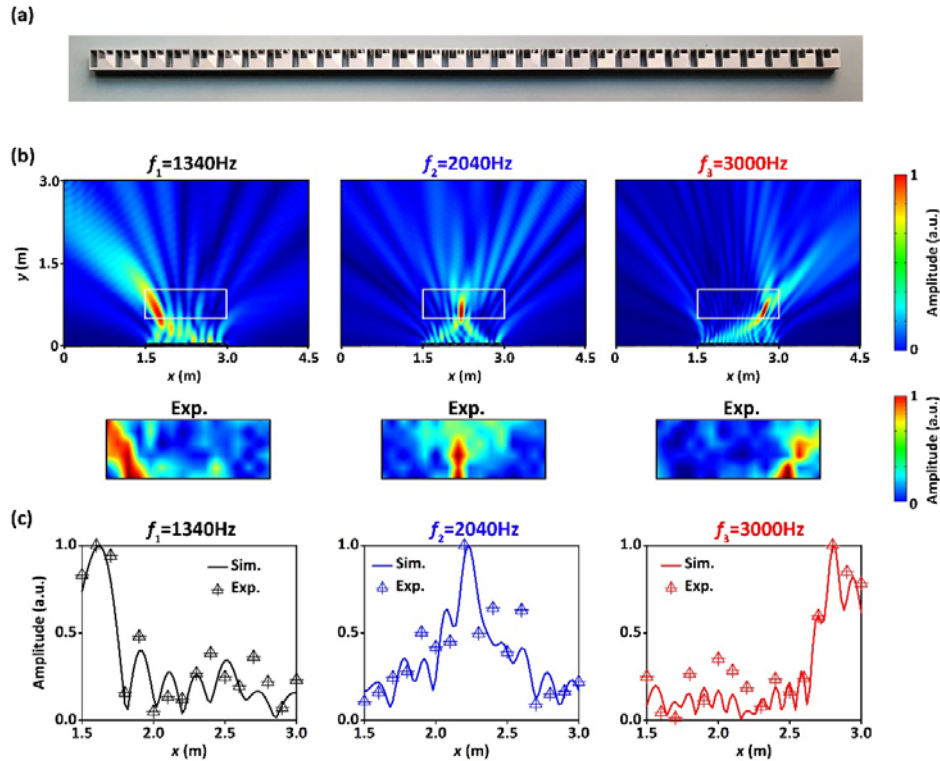


FIG. 5. (a) The sample of the MAM for acoustic focusing with different focal positions ((1.67m, 0.6m), (2m, 0.6m), and (2.33m, 0.6m)) at 1340Hz, 2040Hz, 3000Hz, respectively. (b) The simulated and experimental acoustic pressure distributions of the

acoustic focusing at three frequencies. The measured results of the acoustic pressure fields at the given region marked in the figure are shown in the inset. (c) The simulated and the measured results of the acoustic pressure amplitude distributions at the line of  $y = 0.6\text{m}$ .

## VI. SUMMARY

In conclusion, we have demonstrated a 2D multifunctional and multi-frequency acoustic metasurfaces with achromatic manipulation or mixed functionalities. The design of the metasurface supercell is simple and can be easily fabricated with only one material. The geometry of the structure can be further optimized to achieve different and additional functionalities at different working frequencies. The proposed multifunctional metasurface may pave the way and lead to various unusual and contemporary applications, such as functional device with special dispersion property [26], multiple beam shaping [27] and energy harvesting [12, 28].

## ACKNOWLEDGMENTS

We would like to thank Dr. Jingkai Weng for helpful discussions. This work is supported by the Air Force Office of Scientific Research under award number FA9550-18-1-7021, by la Région Grand Est and by Institut Carnot ICEEL.

## References

[1] N. F. Yu, P. Genevet, M. A. Kats, F. Aieta, J. P. Tetienne, F. Capasso, and Z. Gaburro,

Science **334**, 333–337 (2011).

[2] B. Assouar, B. Liang, Y. Wu, Y. Li, J. C. Cheng, and Y. Jing, Nat. Rev. Mater. **3**, 460–472 (2018).

[3] Y. Li, B. Liang, Z. M. Gu, X. Y. Zou, and J. C. Cheng, Sci. Rep. **3**, 2546 (2013).

[4] Y. Li, X. Jiang, B. Liang, J. C. Cheng, and L. K. Zhang, Phys. Rev. Applied **4**, 024003 (2015).

[5] G. C. Ma, M. Yang, S. W. Xiao, Z. Y. Yang, and P. Sheng, Nat. Mater. **13**, 873–878 (2014).

[6] X. F. Zhu, K. Li, P. Zhang, J. Zhu, J. T. Zhang, C. Tian, and S. C. Liu, Nat. Commun. **7**, 11731 (2016).

[7] Y. F. Zhu, X. Y. Zou, B. Liang, and J. C. Cheng, Appl. Phys. Lett. **107**, 113501 (2015).

[8] Y. Li, S. B. Qi, and B. Assouar, New J. Phys. **18**, 043024 (2016).

[9] M. Amin, O. Siddiqui, W. Orfali, M. Farhat, and A. Khelif, Phys. Rev. Applied **10**, 064030 (2018).

[10] B. Y. Liu, W. Y. Zhao, and Y. Y. Jiang, Sci. Rep. **6**, 38314 (2016).

[11] J. F. Li, W. Q. Wang, Y. B. Xie, B. I. Popa, and S. A. Cummer, Appl. Phys. Lett. **109**, 091908 (2016).

[12] G. S. Liu, Y. Y. Peng, M. H. Liu, X. Y. Zou, and J. C. Cheng, Appl. Phys. Lett. **113**, 153503 (2018).

[13] Y. F. Zhu, X. D. Fan, B. Liang, J. C. Cheng, and Y. Jing, Phys. Rev. X **7**, 021034 (2017).

[14] Y. F. Zhu, X. D. Fan, B. Liang, J. Yang, J. Yang, L. L. Yin, and J. C. Cheng, AIP



Advances **6**, 121702 (2016).

[15] X. Chen, P. Liu, Z. Hou and Y. Pei. Appl. Phys. Lett. **110**, 161909 (2017).

[16] Y. Li and B. Assouar, Appl. Phys. Lett. **108**, 063502 (2016).

[17] S. Qi and B. Assouar, J. Appl. Phys. **123**, 234501 (2018).

[18] H. Esfahlani, S. Karkar, H. Lissek, and J. R. Mosig, Phys. Rev. B **94**, 014302 (2016).

[19] C. Faure, O. Richoux, S. Felix, and V. Pagneux, Appl. Phys. Lett. **108**, 064103 (2016).

[20] M. Dubois, C. Shi, Y. Wang, and X. Zhang, Appl. Phys. Lett. **110**, 151902 (2017).

[21] L. Kinsler, Fundamentals of Acoustics (Wiley, New York, 1982).

[22] T. A. Johansson and M. J. Kleiner, J. Acoust. Soc. Am. **34**, 110, 1315-1328 (2001).

[23] Y. Cheng, J. Y. Xu, and X. J. Liu, Phys. Rev. B **77**, 045134 (2008).

[24] See Supplemental Material at [LINK](#) for the correctional neck length of 2D Helmholtz resonator, and the calculation of mutual impedance.

[25] F. Aieta, M. A. Kats, P. Genevet, and F. Capasso, Science **347**, 1342-1345 (2015).

[26] Y. F. Zhu, X. Y. Zou, R. Q. Li, X. Jiang, J. Tu, B. Liang, and J. C. Cheng, Sci. Rep. **5**, 10966 (2015).

[27] Y. F. Zhu, J. Hu., X. D. Fan, J. Yang, B. Liang, X. F. Zhu, and J. C. Cheng. Nat. Commun. **9**, 1632 (2018).

[28] S. B. Qi, Y. Li, and B. Assouar, Phys. Rev. Applied **7**, 054006 (2017).